In vivo properties of Arabidopsis FCA condensates involved in RNA 3' processing

Geng-Jen Jang[1], Alex L. Payne-Dwyer[2], Robert Maple[1], Zhe Wu[1,3], Fuquan Liu[1,4], Sergio G. Lopez[1], Yanning Wang[5], Xiaofeng Fang[5], Mark C. Leake[2,6] and Caroline Dean[1,*]

[1]Department of Cell and Developmental Biology, John Innes Centre, Norwich, UK

[2]School of Physics, Engineering and Technology, University of York, York, UK

[3]Institute of Plant and Food Science, Southern University of Science and Technology, Shenzhen, China

[4]Institute of Global Food Security, Queen's University Belfast, Belfast, UK

[5]Center for Plant Biology, Tsinghua University, Beijing, China.

[6]Department of Biology, University of York, York, UK

*Corresponding author, Tel: +44 (0)1603 450000; E-mail: caroline.dean@jic.ac.uk

Keywords: biomolecular condensate, RNA processing, *FLC*, *COOLAIR*, noncoding RNA

Abstract

Our understanding of the functional requirements underpinning biomolecular condensation *in vivo* is still relatively poor. The Arabidopsis RNA binding protein FCA is found in liquid-like nuclear condensates that function in RNA 3' processing, promoting proximal polyadenylation at many targets in the Arabidopsis genome. To further understand the properties of these condensates *in vivo* we used single particle tracking experiments on FCA stably expressed at endogenous levels in plant nuclei. These revealed FCA forms a core tetramer that multimerizes into higher-order particles, corresponding to condensates observed using confocal microscopy. The coiled-coil protein FLL2, which is genetically required for FCA function and condensate formation, showed co-localization primarily to the larger condensates. A missense mutation in the FCA RRM domain, also identified in a genetic screen, reduced the average FCA condensate size but had no influence on core FCA tetramer formation. Our work points to a modular structure for FCA condensates centred around a core of four FCA molecules, which multimerize to larger functionally important condensates via associated RNA and FLL2 interaction.

Introduction

Cellular compartmentalization by biomolecular condensates is associated with diverse processes in eukaryotic cells (Banani *et al*, 2017; Shin & Brangwynne, 2017). While *in vitro* studies have highlighted their roles in increasing local concentration and residence time of interacting components, the functional characteristics of heterogeneous condensates *in vivo* remain unclear. Plants are an excellent system in which to study biomolecular condensates (Field *et al*, 2023). For example, Arabidopsis *FLOWERING LOCUS C* (*FLC*), a gene encoding a key flowering repressor, is regulated by co-transcriptional and antisense-mediated chromatin silencing mechanisms (Fang *et al*, 2020; Xu *et al*, 2021) that involve multiple nuclear biomolecular condensates with very different properties (Berry *et al*, 2017; Fang *et al*.,

2019; Zhu *et al*, 2021; Fiedler *et al*, 2022). One of those involves the RNA-binding protein FCA, which forms liquid-like nuclear condensates (Fang *et al*, 2019). Another involves FRIGIDA, a strong activator of *FLC* expression, which forms condensates at low temperature, with dynamics that are slow compared to FCA (Zhu *et al*, 2021). FCA directly interacts with FY, a Pfs2p/WDR33 homologue and a central component of the polyadenylation machinery in eukaryotes (Simpson *et al*, 2003). FCA contains two RRM (RNA Recognition Motif) domains and a WW domain located between two predicted prion-like domains (Macknight *et al*, 1997). FCA recruits RNA 3' processing factors to R-loops and other chromatin tangles to induce transcription-coupled chromatin repression (Xu *et al*., 2021; Mateo-Bonmati *et al*., 2024; Menon *et al*., 2024). This mechanism also involves a coiled-coil protein, FLL2, required for the liquid-liquid phase separation of FCA nuclear condensates and *FLC* repression (Fang *et al*, 2019). *In vitro* assays revealed that FCA condensates were enhanced by addition of low amounts of Arabidopsis RNA. However, the immunoprecipitation of *COOLAIR* nascent transcripts by FCA was not dependent on FLL2 (Fang *et al*, 2019).

Knowledge of the properties and molecular structure of biomolecular condensates helps dissection of the molecular mechanisms involved (Peran and Mittag, 2020). However, studies of biological condensates have focused on *in vitro* analysis and transfection studies and if *in vivo* stable expression fusions have been made they are often not carefully matched to endogenous expression levels. This will influence the *in vivo* biophysical properties. Here, we therefore generated stable transgenic plants with fusions expressed under their own regulatory regions and chose lines that expressed the fusion at endogenous levels. Determining the biophysical properties of condensates *in vivo* in plant systems is challenging so we exploited SlimVar microscopy, a single-molecule imaging technique (Plank *et al*., 2009; Payne-Dwyer *et al*, 2024). This enables simultaneous tracking of individual molecules within a wide range of biological condensates providing quantitative measurements of molecule number and molecular motion behaviour (Shen *et al*, 2023). It has been used to study biomolecular condensates in live cells including bacteria, yeast or mammalian cells (Kent *et al*, 2020; Izeddin *et al*, 2014; Ladouceur *et al*, 2020; Biswas *et al*, 2022) and we adapted it for living plant tissues to specifically study nuclear proteins (Bayle *et al*, 2021).

Our findings indicate that FCA condensates consist of multimers of a tetrameric FCA core, with sizes ranging from approximately 16 to 56 molecules. The lower diffusion coefficient of the larger particles, compared to core particles, suggests they correspond to the liquid-like condensates observed using confocal microscopy. Notably, FLL2, essential for FCA function, predominantly co-localizes within the larger condensates. The involvement of RNA in promoting FCA condensation was shown through the identification of a missense mutation in the FCA second RRM domain. This mutation reduced RNA-binding activity *in vitro*, significantly attenuated FCA condensate formation, lowered RNA 3' processing efficiency and prevented *FLC* repression but did not influence the core tetramer. Our work

points to a modular structure for FCA and RNA 3' processing condensates, with a core of four FCA molecules that multimerize via associated RNA and FLL2 interaction to larger functionally important condensates.

Results

Single particle tracking reveals physical properties of FCA condensates.

For the SlimVar microscopy and co-localization analysis we chose to generate an FCA-mScarlet-I translational fusion. mScarlet-I is a bright red fluorescent protein known for its characteristics as a rapidly maturing monomer (Bindels *et al*, 2016). A mScarlet-I coding sequence was inserted into an FCA genomic clone and transgenic plant lines were generated, where the fusion was expressed at similar level as the endogenous FCA gene (Fig EV1A and B). The FCA mScarlet-I fusion formed liquid-like condensates (Fig 1A) and rescued the *fca-9* mutant phenotype (Fig EV1B), just like the FCA-GFP fusion. SlimVar microscopy provided the capability to track very small FCA particles dynamically on whole root tissue as it incorporates an oblique illumination angle of 60 ± 5°degrees to enhance imaging contrast (Fig 1A). The single-molecule sensitivity of SlimVar *in vivo*, coupled with stepwise photobleaching of fluorescent protein tags (Leake *et al*, 2006; Reyes-Lamothe *et al*, 2010; Payne-Dwyer et al, 2024), enabled accurate quantification of the number of FCA molecules (stoichiometry) within the nuclear condensates in intact tissue (Fig EV2; Jin *et al*, 2021).

Analysis of the single particle tracking dataset identified a distinct peak representing approximately 4 molecules of FCA (Fig 1B) with other peaks in multiples of 4 from approximately 16 to 56 molecules. To investigate whether these regular peaks follow specific patterns, we calculated the periodicity using the nearest-neighbour peak intervals. (Payne-Dwyer *et al*, 2024). The estimate of the number of molecules in a repeat unit depends on consistent stoichiometry intervals observed between nearest-neighbour peaks in the stoichiometry distribution. The periodicity peaks for FCA particles were found to be approximately 4.2 and 8.7 (Fig 1C). To determine whether tetramerization is intrinsic to FCA, we purified recombinant FCA truncated proteins and tested the size with size exclusion chromatography with multi-angle static light scattering (SEC-MALS). The FCA N-terminal region containing RRM domains (Fang *et al*., 2019) forms trimers or tetramers, while the C-terminal region containing prion-like domains forms megacomplexes of more than 100 molecules (Fig EV3). These results suggest that the core module of an FCA particle is a tetramer, with larger condensates forming through the higher-order assembly of these tetrameric units.

We analysed the diffusion coefficient of individual particles with different stoichiometry. Generally, particles with low stoichiometry display variable mobility, while those with high stoichiometry show

low mobility (Fig 1D). In particular, the diffusion coefficient of particles with stoichiometry less than 10 or more than 10 is 0.54±0.75 (mean ± s.d.) and 0.26 ± 0.4, respectively.

FCA and FLL2 predominantly co-localize in the larger size class of condensates.

Our previous study used transient assays suggested that FCA condensates serve as the sites for the interaction between FCA, FLL2 and 3'-end processing factors (Fang *et al*, 2019). However, the condensates formed by FCA and FLL2 exhibited different patterns in low resolution images of Arabidopsis roots (Fang *et al*, 2019). To investigate the potential co-localization of FCA and FLL2 within the same nuclear condensates *in vivo*, we crossed plants carrying an FCA-mTurquoise2 transgene (Xu *et al*, 2021) with plants carrying FLL2-eYFP transgene (Fang *et al*, 2019) and used F3 plants expressing both reporters for imaging. Utilizing 3D imaging and Airyscan confocal microscopy, we found that FCA and FLL2 generally reside in distinct condensates within the cell nucleus (Fig 2A) but co-localize within a few larger condensates (Fig 2B and D). We conducted a comprehensive analysis to determine the size distributions for FCA, FLL2 and FCA/FLL2-co-localized condensates (Fig 2C). The data suggest a specific association between FCA and FLL2 within larger condensates.

To address if these prominent FCA/FLL2 condensates directly associate with the *FLC* locus, we crossed the FCA-mScarlet-I transgene into a line carrying a previously established *FLC-lacO*/LacI-eYFP system enabling spatial localization of the *FLC* locus in the nucleus. This line also carries an active *FRIGIDA* allele so *FLC* is highly transcribed (Rosa *et al*, 2013). FCA condensates did not frequently co-localize with the *FLC-lacO*/LacI-eYFP marked locus (Fig EV4). Only 2.9% of identified FCA condensates and 4.5% of identified *FLC-lacO*/LacI-eYFP loci partially co-localized in 4 of 18 nuclei. This result suggests that FCA condensates only transiently associate with the *FLC* locus in this genotype and environmental conditions. However, it will be interesting to repeat this analysis in a genotype where *FLC* is transcriptionally repressed by FCA, but where the Polycomb silencing has not yet been triggered (Menon *et al*, 2024).

FCA condensation is dependent on a functional RRM domain.

To further investigate the functional significance of the molecular composition in FCA condensates we continued a genetic screen for factors essential for FCA function (Liu *et al*, 2007). This identified a missense mutation on the FCA overexpression transgene at amino acid 304 of the FCA protein, resulting in a leucine to phenylalanine change (Fig EV1C). This alteration is located within the second RRM domain of FCA, a domain conserved across various species (Macknight *et al*, 1997; Fig EV1D). That the mutant came out of an *FLC* mis-expression screen and exhibited late flowering shows the RNA-binding activity is important for FCA function (Fig EV1E). The impact of this missense mutation on the RNA-binding activity was established through *in vitro* RNA-binding assays (Fig EV1F).

147

148 To examine whether this RRM mutation affects FCA condensation, we generated transgene constructs
149 expressing an FCA wild-type genomic DNA fragment with (FCArrm) and without (FCAwt) the RRM
150 mutation fused with mScarlet-I and introduce them into *fca-9* mutant (Fig EV1A). After selecting for
151 single insertion transgenic plants and homozygotes, we analysed the FCAwt condensates within the
152 nuclei of young roots using Airyscan confocal microscope. Plants containing the FCArrm transgene
153 limited the size and number of condensates, displaying a more diffuse signal compared to plants
154 carrying FCAwt (Fig 3A and B).

155

156 In order to determine whether the RRM mutant alters the structure of FCA condensates, we also
157 conducted single particle tracking with the FCArrm lines. We observed an obvious stoichiometry peak
158 of approximately 4 molecules for FCArrm, slightly higher than that for FCAwt (Fig 3C; Appendix Fig
159 S1). However, when focusing on particles with stoichiometries exceeding 8 molecules, the probability
160 density of FCArrm was found to be lower than FCAwt. FCArrm particles with more than 16 molecules
161 were scarce, however, the integrated nuclear intensity of fluorescent signal in FCArrm and FCAwt
162 showed no obvious change (Appendix Fig S2). This result suggests that the reduced RNA-binding
163 activity of FCA proteins decreases their likelihood of forming larger particles with a range of 16 to 56
164 molecules, consistent with the confocal imaging analysis.

165

166 To determine if the RRM mutant changed the physical properties of FCA condensates, we compared
167 the diffusion coefficients of individual particles with their stoichiometry (Fig 3D). The mean
168 stoichiometry of FCArrm is lower than that of FCAwt, while the overall pattern of diffusion coefficients
169 is distributed towards slightly higher values (Fig 3E; Appendix Fig S3). Surprisingly, the periodic unit
170 of FCArrm only experiences a minor reduction compared to FCAwt, which implies that FCA proteins
171 with reduced RNA-binding activity retain the capacity to form the tetrameric core (Fig 3F). Thus, the
172 RNA-binding activity of FCA proteins affects the formation of larger condensates but does not affect
173 core protein assembly.

174

175 **The functional RNA-binding domain is required for *COOLAIR* R-loop resolution and FCA auto-**
176 **regulation.**

177 We then used the FCAwt and FCArrm lines to further investigate the functional importance of RNA
178 binding. Compared to the FCAwt transgenic plants, FCArrm plants displayed higher levels of *FLC*
179 expression and therefore flowered late (Fig 4A and B, EV1B). FCA associates with *COOLAIR*,
180 recruiting 3' processing factors to promote proximal *COOLAIR* polyadenylation, thus resolving a
181 *COOLAIR*-formed R-loop (Liu *et al*, 2010; Xu *et al*, 2021). The ratio of proximal-to-distal isoforms of
182 *COOLAIR* transcripts was reduced in the FCArrm lines compared to FCAwt consistent with reduced

R-loop resolution when RNA binding is defective (Fig 4C). S9.6-DNA/RNA immunoprecipitation followed by cDNA conversion (DRIPc)-qPCR analysis showed higher R-loop level in FCArrm relative to FCAwt, indicating that FCArrm has reduced ability to resolve the *COOLAIR*-induced R-loop (Fig 4D).

FCA autoregulates itself promoting polyadenylation at the proximal sites in intron 3 (Quesada *et al*, 2003), so we conducted Quant-seq analysis (Moll *et al*., 2014) to capture polyadenylated *FCA* transcripts in Col-0, FCAwt, FCArrm and *fca-9.* In FCArrm and *fca-9*, there were significantly fewer reads of transcripts corresponding to proximally polyadenylated *FCA* transcripts compared to FCAwt and Col-0. Conversely, reads at the distally polyadenylated site of *FCA* increased (Fig 5), all consistent with reduced FCA function. RNA-binding activity is thus important for FCA condensation and for well-defined FCA functional roles, promotion of proximal *COOLAIR* termination and R-loop resolution.

Discussion

Our study provides insight on the functional properties of the dynamic liquid-like RNA 3' processing condensates containing the Arabidopsis nuclear RNA-binding protein FCA. We conducted single particle tracking to determine the molecular stoichiometry and diffusivity of FCA condensates in plant nuclei. This revealed insights into the particle size and association of FCA with its protein and RNA partners functioning in *FLC* repression. Our work points to a modular structure for FCA condensates centred around a core of four FCA molecules, which multimerize to larger functionally important condensates via associated RNA and FLL2 interaction.

The missense mutation in the FCA RRM domain reduced RNA-binding activity, attenuated condensate formation and prevented *FLC* repression but the stoichiometry of the smaller FCA particles was unaffected. The core modular structure of FCA particles is reminiscent of findings for ELAV, a well-characterized Drosophila RNA-binding protein with three RRM domains. ELAV tetramerizes on its target RNAs to form a defined complex (Soller & White, 2005). The role of RNA in the larger FCA condensate formation may involve the functionality of a hydrophobic core in the RRM domain. The missense mutation (L304F) in the FCA second RRM domain is positioned within an equivalent hydrophobic region to that recently found to influence the protein stability of TDP-43, an amyotrophic lateral sclerosis (ALS)-linked RNA binding protein (Mackness *et al*, 2024). The L304F change would strengthen the hydrophobic core but further structural analysis of RRM domains will be important to dissect this further. The FCA protein has many domains- two prion-like domains (Chakrabortee *et al*, 2016), two RRM domains (Macknight *et al*, 1997), a WW domain (Simpson *et al*, 2003; Henderson *et al*, 2005) and an extended NH2 terminus that initiates translation with a CTG (non-methionine) start codon (Simpson *et al*, 2010). These may all participate in the modular multimerization.

RNA methylation may also be a contributing factor to the condensation dynamics as m6A has been shown to function in the regulatory mechanisms of *FLC* and *COOLAIR* (Xu *et al*, 2021; Wang *et al*, 2022; Sun *et al*, 2022; Amara *et al*, 2023). We therefore need to understand if the dynamic structures are affected by RNA modification and how the FCA tetramer interfaces with its target RNAs. Continued analysis of the role of the first RRM may also be productive as the protein phosphatase SSU72 was found to antagonize FCA's binding to *COOLAIR* in a manner dependent on the first RRM motif and its flanking region (Tian *et al*, 2019). Reversible protein phosphorylation is a pivotal mechanism in governing the (dis)assembly of biomolecular condensates in cellular processes (Sridharan *et al*, 2022). Lastly, any posttranslational modification of the FCA protein may also influence RNA binding or modular multimerization.

COOLAIR transcripts form dense 'clouds' at each *FLC* locus as judged by single-molecule fluorescence in situ hybridization, which are enhanced upon cold exposure (Rosa *et al*, 2016). Whether the FCA condensates associate with these *COOLAIR* clouds will require RNA live imaging analysis. It is interesting to speculate that *COOLAIR* molecules might undergo thermo-responsive phase transitions as has been found recently for other RNAs (Wadsworth *et al*, 2023). Protein partners can tune this phase behaviour (Ruff *et al*, 2020), so this system has a lot of potential to uncover fundamental principles of condensate functionality *in vivo*. In mammalian cells, Mediator-bound enhancers only sporadically co-localize with their target loci. This variability in co-localization can be attributed to a dynamic kissing model, where a distal Mediator cluster interacts with the gene only at specific timepoints (Cho *et al*, 2018; Du *et al*, 2024). Furthermore, *FLC* can exist in either a transcriptionally active (with functional FRIGIDA) or inactive (without functional FRIGIDA) state and switching between these states is connected to co-transcriptional RNA processing (Fang *et al*, 2020; Mateo-Bonmati *et al*, 2024; Menon *et al*, 2024). Exploring whether the transient association of FCA condensates with *FLC* locus reflects the transcriptional status of *FLC* will be the next important question.

Our work demonstrates the power of studying biomolecular condensate functionality in genetically tractable systems. Arabidopsis with its extensive genetic resources, ability to make transgenic lines and small, transparent roots is particularly suitable for these studies, as illustrated by our ability to image condensates in living roots with the single-molecule sensitivity of SlimVar. Coupled with stepwise photobleaching we could accurately quantify the number of molecules within condensates providing mechanistic insights into the modular structure of FCA condensates, with and without various functionally important partners. These tools now allow us to explore the role of FCA condensate dynamics in response to various environmental exposures.

Methods

Plant materials and growth conditions

258 The wild type Col-0, *fca-9* mutant allele, *pFCA::FCA-mTurquoise* and *pFLL2::FLL2-eYFP* transgenic
259 plants were described previously (Fang *et al*, 2020; Xu *et al*, 2021). To generate the *pFCA::FCA-*
260 *mScarlet-I* transgenic plants, FCA genomic DNA fragments was amplified and insert into the pENTRY
261 vector. The mScarlet-I coding sequence was inserted before the stop codon via In-Fusion seamless
262 cloning. The FCA genomic DNA fragment fused mScarlet-I was transferred to pSLJ699I5 vector via
263 gateway cloning. The RRM mutation construct is modified from wild-type FCA genomic DNA
264 constructs via In-Fusion seamless cloning. These constructs were transformed into the *fca-9* mutant.
265 Arabidopsis seeds were surface sterilized and sown on standard half-strength Murashige and Skoog (½
266 MS) medium plate without glucose and stratified at 4 °C for 3 days before transferred to long-day
267 conditions (16-h light at 20 °C, 8-h darkness at 16 °C).
268
269 **Confocal microscopy of FCA-mScarlet-I**
270 Plants were grown vertically on half strength MS plates for 4-7 days. Confocal images were acquired
271 on a Zeiss LSM 880 upright microscope equipped with an Airyscan detector. Samples were imaged
272 through a C-Apochromat 63x/NA 1.2 water-immersion objective by exciting them at 561 nm and using
273 the Airyscan detector in super resolution mode. The fluorescence emission arrived at the detector after
274 passing through a filter that allowed wavelengths between 495-550 nm and above 570 nm to pass
275 through. Typically, the voxel size was 0.06 × 0.06 × 0.26 µm (xyz) and the pixel dwell time was 1.78
276 µs. Z-stacks typically comprised 28 slices and spanned a 7.13 µm range for more than 70% of the
277 nucleus. After Airyscan processing, the image analysis was performed in Arivis Vision4D ver. 4.1.0.
278 (Zeiss). The blob finder algorithm was applied to the mScarlet-I channel using a diameter value of 0.35
279 µm, a probability threshold of 45%, and a split sensitivity of 50%. Blob finder is a segmentation
280 algorithm that excels at finding round or spherical objects in 2D or 3D, respectively. It uses a Gaussian
281 scale to identify seeds for the objects and subsequently applies a watershed algorithm to determine the
282 boundaries of the objects. To exclude non-specific identified condensates, a minimum size of 0.03 μm^3
283 and a sphericity of 0.6 Mesh were set during the analysis. Violin plots reflecting the data distribution
284 were produced with GraphPad Prism 10 software.
285
286 **Co-localization analysis of FCA and FLL2**
287 Confocal images were acquired either on the Zeiss LSM 880 microscope mentioned above or a Zeiss
288 LSM 980 confocal microscope. When using the LSM880, line by line sequential acquisition was
289 employed. Samples were imaged through a C-Apochromat 63x/NA 1.2 water-immersion objective and
290 were excited at 458 (mTurquoise) and 514 nm (eYFP). The fluorescence emission of the samples passed
291 through a filter that only allowed wavelengths in the 465-505 nm range and above 525 nm to reach the
292 Airyscan detector, which was operating in super resolution mode. The voxel size was 0.05 × 0.05 ×
293 0.21 µm (xyz) and the pixel dwell time was 0.72 µs. Z-stacks comprised 25 slices spanning a 4.96 µm
294 range. 0.2 mm TetraSpeck microspheres (Thermo Fisher) were imaged using these same settings and

295 the resulting images were used to correct the sample images for chromatic aberration. The correction
296 was performed in Zen (Zeiss, Germany) using the channel alignment method.
297 After Airyscan processing, channel alignment, and nuclei segmentation, the image analysis was
298 performed in Arivis Vision4D ver. 4.1.0. (Zeiss). Firstly, the blob finder algorithm was applied to the
299 mTurquoise2 channel using a diameter value of 0.35 mm, a probability threshold of 60%, and a split
300 sensitivity of 50%. Then, the blob finder algorithm was applied to the eYFP channel using a diameter
301 value of 0.30 mm, a probability threshold of 50%, and a split sensitivity of 50%. Afterwards, the
302 intersection between the output of the two blob finder operations was calculated. Finally, metrics such
303 as volume, mean intensity, and total intensity were computed for the objects generated by each of the
304 blob finder operations, as well as for their intersection. Violin plots and x-y plots reflecting the data
305 distribution were produced with GraphPad Prism 10 software.
306
307 **SlimVar microscopy**
308 The customized SlimVar microscope was previously described (Payne-Dwyer *et al*, 2024). Continuous
309 wave lasers (Coherent OBIS) delivered a de-expanded Gaussian beam mode (TEM00) to the back
310 aperture of an NA 1.49 Apo TIRF 100× oil immersion objective lens (Nikon). Single molecule
311 sensitivity was achieved using a fast sCMOS camera (Photometrics Prime95B) which triggered a
312 continuous wave laser for 10 ms exposure per frame at 80 Hz. Excitation and emission filters were
313 tailored to mScarlet-I (594/25 nm) for their respective red channels. The total magnification was
314 approximately 200×, resulting in an oversampled image pixel edge size of 53 nm. Nuclei were identified
315 using brightfield mode to determine the best focus and were subsequently captured for manual
316 segmentation later. Fluorescence acquisition settings in the green and red channels were pre-optimized
317 to prevent initial saturation and to ensure the detection of individual molecular brightness tracks for
318 mScarlet-I. These settings were then locked to prevent systematic variation in the characteristic single
319 molecule brightness.
320
321 **Single particle tracking and intensity analysis**
322 Fluorescent particles were identified from SlimVar image sequences and linked into tracks using
323 ADEMScode software (Plank *et al*, 2009). Each of these particles were localised to a super-resolved,
324 subpixel precision, typically 40 nm. The random overlap probability was estimated using a nearest
325 neighbour distance approach (Payne-Dwyer *et al*, 2024). Analysis was spatially restricted to data lying
326 within a region of effectively uniform laser illumination (80% ± 9% s.d. peak intensity) by cropping
327 images to an area of 240 × 184 pixels (12.7 × 9.8 μm). Fluorescence image sequences were further
328 cropped to specify individual nuclei, using manually segmented masks from brightfield images.
329 The 2D diffusion coefficient of each track (D) was computed using the increase of mean-square
330 displacement across time interval according to a random walk model (Leake *et al*, 2008). Focus
331 intensity was calculated by summing the pixel values within a 5-pixel distance and subtracting an

332 averaged background level from the rest of a 17-pixel square (Leake *et al*, 2008). The track
333 stoichiometry was found by extrapolating the first 5 particles intensities to account for photobleaching
334 (Syeda *et al*., 2019), then dividing this initial intensity by the characteristic single molecule brightness
335 (Wollman *et al*., 2017). The characteristic single molecule brightness linked to each reporter was
336 determined as 110 ± 15 (mean ± sem) for mScarlet-I based on the Chung-Kennedy-filtered terminal
337 intensity of tracks in each acquisition (Leake *et al*, 2003), thus providing an internal calibration for track
338 stoichiometry, periodicity, and nuclear protein copy number.
339
340 To calculate periodicity, the stoichiometries of all tracks within each nucleus were represented as a
341 kernel density distribution (Leake *et al*, 2014), employing an empirical standard deviation of 0.6
342 molecules on the characteristic single molecule brightness. Peaks within this distribution were identified
343 using the MATLAB *findpeaks* function, and the intervals between nearest neighbour peaks were
344 computed (Payne-Dwyer *et al*, 2024). Raw estimations of the total number of molecules in each nucleus
345 were determined using ImageJ macros to integrate the pixel values inside segmented nuclei as in
346 previous work (Wollman and Leake, 2015; Payne-Dwyer *et al*, 2024). The nuclear protein copy number
347 of each reporter dataset was refined to exclude autofluorescence by calculating the difference between
348 mean integrated nuclear intensities of the labelled dataset and an unlabeled control, adjusted
349 proportionally to the ratio of mean nuclear segment areas.
350
351 ***In vitro* protein expression and purification**
352 MBP-FCA-RRM and MBP-FCA-PrLD proteins were expressed and purified from *Escherichia coli*
353 (Rosetta) cells using Ni-NTA resin as described previously (Fang *et al*, 2019). Briefly, protein
354 expression was induced by 0.4 mM isopropyl-β-D-1-thiogalactopyranoside (IPTG) at 18°C overnight.
355 Cells were collected by centrifugation and re-suspended in lysis buffer (40 mM Tris-HCl pH7.4, 500
356 mM NaCl, 10% glycerol). The suspension was sonicated for 20 min (3 s ON, 3 s OFF, SCIENTZ) and
357 centrifuged at 13000 *g* for 30 min at 4°C. The supernatant was incubated with Ni-NTA agarose for 20
358 min, washed and eluted with buffer E (40 mM Tris-HCl pH7.4, 500 mM NaCl, 500 mM Imidazole,
359 Sangon). Proteins were further purified by gel filtration chromatography (Superdex-200; GE Healthcare)
360 and stored in buffer S (40 mM Tris-HCl pH7.4, 500 mM NaCl, 1 mM DTT) at −80 °C.
361
362 **Size-exclusion chromatography coupled with multi-angle laser light scattering (SEC-MALS)**
363 Multi-angle light scattering experiments were performed in 40 mM Tris-HCl pH7.4 and 500 mM NaCl
364 using a Superdex-200 10/300 GL size exclusion column (GE Healthcare). The concentration of MBP-
365 FCA-RRM and MBP-FCA-PrLD used was 2 mg/mL. The chromatography system was connected to a
366 Wyatt DAWN HELEOS laser photometer and a Wyatt Optilab T-rEX differential refractometer. Wyatt
367 ASTRA 7.3.2 software was used for data analysis.
368

369 **Expression analysis**

370 Total RNA was extracted from plant materials as described previously (Qüesta *et al*, 2016), treated with
371 TURBO DNase (Ambion) to eliminate DNA contamination, and reverse-transcribed using SuperScript
372 IV Reverse Transcriptase (Invitrogen) with gene-specific reverse primers. Quantitative PCR (qPCR)
373 analysis was conducted on a LightCycler480 II (Roche), and the qPCR data were normalized to the
374 reference genes *UBC* and *PP2A*. To measure the proximal ratio of *COOLAIR*, the level of the proximal
375 component was normalized to the distal *COOLAIR*. Primers were listed in Appendix Table S1.

376

377 **DNA−RNA hybrid immunoprecipitation followed by cDNA conversion (DRIPc)**

378 The DRIP protocol is as described previously (Xu *et al*, 2021) with modifications. In all, 3 g 10-day-
379 old seedlings were harvested and grounded into a fine powder. The powder was suspended in 35 mL of
380 Honda buffer (20mM HEPES, 0.44M sucrose, 1.25% Ficoll, 2.5% dextran T40, 10mM $MgCl_2$, 0.5%
381 Triton x-100, 5 mM DTT, 1x protease inhibitor cocktail (Roche), filtered through one layer of Miracloth,
382 and centrifuged at 3500×g for 15 min. Nuclear pellets were resuspended in 1mL Honda buffer and
383 centrifuged at 8000×g for 1 min. Pellets were then resuspended in the lysis buffer (50mM Tris-HCl pH
384 8.0, 10mM EDTA, 1% SDS) supplied with 0.1 mg/mL proteinase K (AM2546, Invitrogen) and digested
385 at 55 °C overnight with gentle rotation. The mixture was phenol/chloroform extracted, followed by
386 nucleic acid precipitation with NaOAc and ethanol. The nucleic acid pellet was dissolved in water and
387 quantified with Qubit DNA quantification kit (Invitrogen). In general, 1 μg of nucleic acid was digested
388 by restriction enzymes including DdeI, NdeI and XbaI (NEB) overnight. The digested nucleic acid was
389 phenol/chloroform extracted, followed by nucleic acid precipitation with NaOAc and ethanol. Then the
390 nucleic acid was treated with RNAse III (Ambion) and then extracted by phenol/chloroform and ethanol
391 precipitation. The treated nucleic acid was then diluted ten times with dilution buffer (16.7mM Tris pH
392 7.5, 167mM NaCl, 2.2mM EDTA, 0.1% Triton X-100) and 10% was stored at −20 °C as input. In all,
393 5 μg of S9.6 antibody (1:100 dilution, ENH001, Kerafast) was added, then incubated overnight at 4 °C.
394 The next day, 50 μl Protein G Agarose (Invitrogen) was added and incubated for another 2 h. The
395 immunoprecipitants were washed five times with dilution buffer and twice with TE buffer, then were
396 eluted in 100 μl elution buffer (10mM Tris pH 7.5, 2 mM EDTA, 0.2% SDS, 100 ng/μl tRNA) at 55 °C
397 for 2 hours, together with input samples. The nucleic acids were precipitated with NaOAc, isopropanol,
398 and glycogen, dissolved in water. The nucleic acid samples were then treated with treated with TURBO
399 DNase (Ambion) to eliminate DNA contamination, and reverse-transcribed using SuperScript IV
400 Reverse Transcriptase (Invitrogen) with gene-specific reverse primers. All the samples including inputs
401 were subjected to qPCR analysis via LightCycler480 II (Roche). The data were normalized to 1% of
402 input. Primers were listed in Appendix Table S1.

403

404 **Quant-seq**

405 The Quant-seq protocol is as described previously (Mateo-Bonmatí *et al*, 2024). The total RNAs
406 prepared for Quant-seq underwent purification using the Qiagen RNeasy miniprep kit (74106). Lexogen
407 GmbH (Austria) conducted the library preparation, sequencing, and data analysis. Sequencing-ready
408 libraries were created from 100 ng of input RNA using a QuantSeq 3' mRNA-Seq Library Prep Kit
409 REV for Illumina (015UG009V0271), following standard procedures. The RNA integrity and quality
410 of indexed libraries were assessed on a Fragment Analyzer device (Agilent Technologies) using a DNF-
411 471 RNA Kit and HS-DNA assay, respectively. Library quantification was carried out using a Qubit
412 dsDNA HS assay (Thermo Fisher).
413 A sequencing-ready pool of indexed libraries was then sequenced on an Illumina NextSeq 2000 with a
414 100-cycle cartridge, using the Custom Sequencing Primer (CSP). Verification of read quality utilized
415 FastQC version v0.11.7, and read adapter trimming employed cutadapt version 1.18 (Martin, 2011).
416 Clean reads were mapped to the latest version of the Arabidopsis genome (TAIR10) using the splice-
417 aware aligner STAR version 2.6.1a (Dobin *et al*, 2013).
418
419 **Electrophoretic Mobility Shift Assay**
420 FCA cDNA with L304F mutation was amplified from the mutant as described in Figure EV1.
421 To generate RNA probes, dsDNA of the corresponding region was amplified through PCR (primers see
422 Appendix Table S1) with the T7/T3 phage polymerase promoter added at the 5' end of the primer.
423 *COOLAIR* RNA was then generated by following a protocol provided by the MAXIscript® T7
424 Transcription Kit (Invitrogen). The resulting product was DNA digested, denatured, and separated on
425 5% TBE gel containing 8 M Urea. The band at the right size was cut out, sliced, and eluted in gel
426 extraction buffer (0.5 M NH4Ac, 1 mM EDTA, 0.2% SDS, 1xRNAsecure™ (Invitrogen)) at 37ºC
427 overnight, followed by precipitation with isopropanol. 10 pmol purified RNA was 3'biotinylated by
428 following the instructions provided by the RNA 3' End Biotinylation Kit (Pierce). The labelling
429 efficiency was determined to be at least 90%. For the gel shift assay, a 20 µl reaction (25 ng/µl protein,
430 2 nM probe, 250 ng/µl tRNA, 50 ng/µl heparin, 10 mM HEPES (pH 7.3), 120 mM KCL, 1 mM $MgCl_2$,
431 1 mM DTT) was set up on ice. For the competition assay, 2x to 100x of unlabelled probe was included
432 in the reaction. The reaction with only GST was used as a negative control. The mixture was incubated
433 at room temperature for 5 min and resolved on 3.5% native TBE-acrylamide gel and transferred onto a
434 positively charged nylon membrane. The biotinylated RNA on the membrane was detected by
435 chemiluminescence according to a protocol provided with the Chemiluminescent Nucleic Acid
436 Detection Module (Pierce, 89880). Primers to generate probes were listed below. For the binding
437 reaction, 1 µg of different recombinant proteins was incubated with 2 pmol of biotinylated probe in 20
438 µL of 1× buffer containing 20 mM Tris (pH 7.5), 100 mM NaCl, 10 mM $MgCl_2$, non-specific
439 competitors (1µg/µl heparin and 5µg tRNA) and 0.05% Triton X-100 at room temperature for 10 min.
440 The RNA-protein mixture was resolved on 6% 1× TBE acrylamide gel under 100 V for 50 min,
441 followed by electrophoretic transfer to positively charged nylon membranes (GE Healthcare). The

biotinylated RNA on the membrane was UV cross-linked and detected using chemiluminescent nucleic acid detection following the manufacturer's instructions (Thermo Fisher).

Data availability

Raw image data of confocal microscopy and co-localization analysis have been deposited in the BioImage Archive (https://www.ebi.ac.uk/biostudies/bioimages/studies/S-BIAD1154). The raw and processed imaging data and analysed tracks of single particle tracking analysis are available at the BioStudies: https://doi.org/10.6019/S-BIAD1234. The ADEMScode MATLAB tracking analysis software can be found at https://github.com/alex-payne-dwyer/single-molecule-tools-alpd.

The raw reads of Quant-seq have been deposited in the Short Read Archive (SRA) under the reference (PRJNA1087342 and PRJNA1076161).

Author contributions

G-J.J. and C.D. conceived the study. G-J.J., A.P.-D., R.M., Z.W., F.L., Y.W., X.F. and S.G.L. performed the investigation and analysed the data. G-J.J. and C.D. wrote the manuscript; all authors reviewed and edited the manuscript. M.C.L. and C.D. supervised the study, acquired the funding, and were the project administrators.

Acknowledgements

We thank Shuqin Chen and Tina Zhang for their excellent technical assistance and Hsuan Pai for her artwork assistance. We also thank all members of the Dean and Howard groups. This work was funded by the European Research Council Advanced Grant (EPISWITCH, 833254), Wellcome Trust (210654/Z/18/Z), and the Royal Society Professorship (RP\R1\180002) to Caroline Dean, and EPSRC grants (EP/T00214X/1 to C.D. and EP/T002166/1 and EP/W024063/1 to M.L).

Conflict of Interest

The authors declare that they have no conflict of interest.

References

Amara U, Hu J, Cai J & Kang H (2023) FLK is an mRNA m6A reader that regulates floral transition by modulating the stability and splicing of *FLC* in Arabidopsis. *Mol Plant* 16: 919–929

Banani SF, Lee HO, Hyman AA & Rosen MK (2017) Biomolecular condensates: Organizers of cellular biochemistry. *Nat. Rev. Mol. Cell Biol.* 18: 285-298

Bayle V, Fiche JB, Burny C, Platre MP, Nollmann M, Martinière A & Jaillais Y (2021) Single-particle tracking photoactivated localization microscopy of membrane proteins in living plant tissues. *Nat Protoc* 16: 1600–1628

Berry S, Rosa S, Howard M, Bühler M & Dean C (2017) Disruption of an RNA-binding hinge region abolishes LHP1-mediated epigenetic repression. *Genes Dev* 31: 2115–2120

Bindels DS, Haarbosch L, Van Weeren L, Postma M, Wiese KE, Mastop M, Aumonier S, Gotthard G, Royant A, Hink MA, *et al* (2016) mScarlet: A bright monomeric red fluorescent protein for

482 cellular imaging. *Nat Methods* 14: 53–56
483 Biswas S, Chen Z, Karslake JD, Farhat A, Ames A, Raiymbek G, Freddolino PL, Biteen JS &
484 Ragunathan K (2022) HP1 oligomerization compensates for low-affinity H3K9me recognition and
485 provides a tunable mechanism for heterochromatin-specific localization. *Sci Adv* 8
486 Chakrabortee S, Kayatekin C, Newby GA, Mendillo ML, Lancaster A & Lindquist S (2016)
487 Luminidependens (LD) is an Arabidopsis protein with prion behavior. *Proc Natl Acad Sci U S A*
488 113: 6065–6070
489 Cho WK, Spille JH, Hecht M, Lee C, Li C, Grube V & Cisse II (2018) Mediator and RNA
490 polymerase II clusters associate in transcription-dependent condensates. *Science* 361: 412–415
491 Dobin A, Davis CA, Schlesinger F, Drenkow J, Zaleski C, Jha S, Batut P, Chaisson M & Gingeras TR
492 (2013) STAR: Ultrafast universal RNA-seq aligner. *Bioinformatics* 29: 15–21
493 Du M, Stitzinger SH, Spille J, Hijaz M, Quintana A, Cisse II, Du M, Stitzinger SH, Spille J, Cho W,
494 et al (2024) Direct observation of a condensate effect on super- enhancer controlled gene bursting.
495 *Cell* 187: 331–344
496 Fang X, Wang L, Ishikawa R, Li Y, Fiedler M, Liu F, Calder G, Rowan B, Weigel D, Li P, *et al*
497 (2019) Arabidopsis FLL2 promotes liquid–liquid phase separation of polyadenylation complexes.
498 *Nature* 569: 265–269
499 Fang X, Wu Z, Raitskin O, Webb K, Voigt P, Lu T, Howard M & Dean C (2020) The 3' processing of
500 antisense RNAs physically links to chromatin-based transcriptional control. *Proc Natl Acad Sci U*
501 *S A* 117: 15316–15321
502 Fiedler M, Franco-Echevarría E, Schulten A, Nielsen M, Rutherford TJ, Yeates A, Ahsan B, Dean C
503 & Bienz M (2022) Head-to-tail polymerization by VEL proteins underpins cold-induced Polycomb
504 silencing in flowering control. *Cell Rep* 41
505 Field S, Jang GJ, Dean C, Strader LC & Rhee SY (2023) Plants use molecular mechanisms mediated
506 by biomolecular condensates to integrate environmental cues with development. *Plant Cell* 35:
507 3173–3186
508 Henderson IR, Liu F, Drea S, Simpson GG & Dean C (2005) An allelic series reveals essential roles
509 for FY in plant development in addition to flowering-time control. *Development* 132: 3597–3607
510 Izeddin I, Récamier V, Bosanac L, Cissé II, Boudarene L, Dugast-Darzacq C, Proux F, Bénichou O,
511 Voituriez R, Bensaude O, *et al* (2014) Single-molecule tracking in live cells reveals distinct target-
512 search strategies of transcription factors in the nucleus. *Elife* 3: 1–27
513 Jin X, Lee JE, Schaefer C, Luo X, Wollman AJM, Payne-Dwyer AL, Tian T, Zhang X, Chen X, Li Y,
514 *et al* (2021) Membraneless organelles formed by liquid-liquid phase separation increase bacterial
515 fitness. *Sci Adv* 7
516 Jumper J, Evans R, Pritzel A, Green T, Figurnov M, Ronneberger O, Tunyasuvunakool K, Bates R,
517 Žídek A, Potapenko A, *et al* (2021) Highly accurate protein structure prediction with AlphaFold.
518 *Nature* 596: 583–589
519 Kent S, Brown K, Yang C hsun, Alsaihati N, Tian C, Wang H & Ren X (2020) Phase-Separated
520 Transcriptional Condensates Accelerate Target-Search Process Revealed by Live-Cell Single-
521 Molecule Imaging. *Cell Rep* 33: 108248
522 Ladouceur AM, Parmar BS, Biedzinski S, Wall J, Tope SG, Cohn D, Kim A, Soubry N, Reyes-
523 Lamothe R & Weber SC (2020) Clusters of bacterial RNA polymerase are biomolecular
524 condensates that assemble through liquid-liquid phase separation. *Proc Natl Acad Sci U S A* 117:
525 18540–18549
526 Leake MC, Wilson D, Bullard B, Simmons RM & Bubb MR (2003) The elasticity of single kettin
527 molecules using a two-bead laser-tweezers assay. *FEBS Lett* 535: 55–60
528 Leake MC, Chandler JH, Wadhams GH, Bai F, Berry RM & Armitage JP (2006) Stoichiometry and
529 turnover in single, functioning membrane protein complexes. *Nature* 443: 355–358
530 Leake MC, Greene NP, Godun RM, Granjon T, Buchanan G, Chen S, Berry RM, Palmer T & Berks
531 BC (2008) Variable stoichiometry of the TatA component of the twin-arginine protein transport
532 system observed by in vivo single-molecule imaging. *Proc Natl Acad Sci U S A* 105: 15376–15381
533 Leake MC (2014) Analytical tools for single-molecule fluorescence imaging in cellulo. *Phys Chem*
534 *Chem Phys* 16: 12635–12647
535 Liu F, Quesada V, Crevillén P, Bäurle I, Swiezewski S & Dean C (2007) The Arabidopsis RNA-
536 Binding Protein FCA Requires a Lysine-Specific Demethylase 1 Homolog to Downregulate *FLC*.

Mol Cell 28: 398–407
Liu F, Marquardt S, Lister C, Swiezewski S & Dean C (2010) Targeted 3′ processing of antisense transcripts triggers Arabidopsis *FLC* chromatin silencing. *Science* 327: 94-7
Mackness BC, Morgan BR, Deveau LM, Kathuria S V., Zitzewitz JA & Massi F (2024) A hydrophobic core stabilizes the residual structure in the RRM2 intermediate state of the ALS-linked protein TDP-43. *bioRxiv* 2024.06.12.598648.
Macknight R, Bancroft I, Page T, Lister C, Schmidt R, Love K, Westphal L, Murphy G, Sherson S, Cobbett C, *et al* (1997) FCA, a gene controlling flowering time in Arabidopsis, encodes a protein containing RNA-binding domains. *Cell* 89: 737–745
Martin M (2011) Cutadapt removes adapter sequences from high-throughput sequencing reads. *EMBnet.journal* 17: 10-12
Mateo-Bonmatí E, Montez M, Maple R, Fiedler M, Fang X, Saalbach G, Passmore LA & Dean C (2024) A CPF-like phosphatase module links transcription termination to chromatin silencing. *Mol Cell* 84: 2272–2286
Menon G, Mateo-Bonmati E, Reeck S, Maple R, Wu Z, Ietswaart R, Dean C & Howard M (2024) Proximal termination generates a transcriptional state that determines the rate of establishment of Polycomb silencing. *Mol Cell* 84: 2255–2271
Moll P, Ante M, Seitz A & Reda T (2014) QuantSeq 3' mRNA sequencing for RNA quantification. *Nat Methods* 11: i–iii
Payne-Dwyer AL, Jang GJ, Dean C & Leake MC (2024) SlimVar : rapid in vivo single-molecule tracking of chromatin regulators in plants. bioRxiv 2024.05.17.594710.
Peran I & Mittag T (2020) Molecular structure in biomolecular condensates. *Curr Opin Struct Biol* 60: 17–26
Plank M, Wadhams GH & Leake MC (2009) Millisecond timescale slimfield imaging and automated quantification of single fluorescent protein molecules for use in probing complex biological processes. *Integr Biol* 1: 602–612
Quesada V, Macknight R, Dean C & Simpson GG (2003) Autoregulation of FCA pre-mRNA processing controls Arabidopsis flowering time. *EMBO J* 22: 3142–3152
Qüesta JI, Song J, Geraldo N, An H & Dean C (2016) Arabidopsis transcriptional repressor VAL1 triggers Polycomb silencing at *FLC* during vernalization. *Science* 353: 485–488
Reyes-Lamothe R, Sherratt DJ & Leake MC (2010) Stoichiometry and architecture of active DNA replication machinery in *Escherichia coli*. *Science* 328: 498–501
Rosa S, De Lucia F, Mylne JS, Zhu D, Ohmido N, Pendle A, Kato N, Shaw P & Dean C (2013) Physical clustering of *FLC* alleles during polycomb-mediated epigenetic silencing in vernalization. *Genes Dev* 27: 1845–1850
Rosa S, Duncan S & Dean C (2016) Mutually exclusive sense-antisense transcription at *FLC* facilitates environmentally induced gene repression. *Nat Commun* 7: 1–7
Ruff KM, Dar F & Pappu R V. (2021) Ligand effects on phase separation of multivalent macromolecules. *Proc Natl Acad Sci U S A* 118
Shen Z, Jia B, Xu Y, Wessén J, Pal T, Chan HS, Du S & Zhang M (2023) Biological condensates form percolated networks with molecular motion properties distinctly different from dilute solutions. *Elife* 12: 1–32
Shin Y & Brangwynne CP (2017) Liquid phase condensation in cell physiology and disease. *Science* 357
Simpson GG, Dijkwel PP, Quesada V, Henderson I & Dean C (2003) FY is an RNA 3′ end-processing factor that interacts with FCA to control the Arabidopsis floral transition. *Cell* 113: 777–787
Simpson GG, Laurie RE, Dijkwel PP, Quesada V, Stockwell PA, Dean C & Macknight RC (2010) Noncanonical translation initiation of the Arabidopsis flowering time and alternative polyadenylation regulator FCA. *Plant Cell* 22: 3764–3777
Soller M & White K (2005) ELAV multimerizes on conserved AU4-6 motifs important for *ewg* splicing regulation. *Mol Cell Biol* 25: 7580–7591
Sonmez C, Bäurle I, Magusin A, Dreos R, Laubinger S, Weigel D & Dean C (2011) RNA 3′ processing functions of Arabidopsis FCA and FPA limit intergenic transcription. P*roc Natl Acad Sci U S A* 108: 8508–8513

592 Sridharan S, Hernandez-Armendariz A, Kurzawa N, Potel CM, Memon D, Beltrao P, Bantscheff M,
593 Huber W, Cuylen-Haering S & Savitski MM (2022) Systematic discovery of biomolecular
594 condensate-specific protein phosphorylation. *Nat Chem Biol* 18: 1104–1114
595 Syeda AH, Wollman AJM, Hargreaves AL, Howard JAL, Bruning JG, McGlynn P & Leake MC
596 (2019) Single-molecule live cell imaging of Rep reveals the dynamic interplay between an
597 accessory replicative helicase and the replisome. *Nucleic Acids Res* 47: 6287–6298
598 Sun B, Bhati KK, Song P, Edwards A, Petri L, Kruusvee V, Blaakmeer A, Dolde U, Rodrigues V,
599 Straub D, *et al* (2022) FIONA1-mediated methylation of the 3'UTR of *FLC* affects *FLC* transcript
600 levels and flowering in Arabidopsis. *PLoS Genet* 18: 1–22
601 Tian Y, Zheng H, Zhang F, Wang S, Ji X, Xu C, He Y & Ding Y (2019) PRC2 recruitment and
602 H3K27me3 deposition at *FLC* require FCA binding of *COOLAIR*. *Sci Adv* 5: 1–12
603 Varadi M, Anyango S, Deshpande M, Nair S, Natassia C, Yordanova G, Yuan D, Stroe O, Wood G,
604 Laydon A, *et al* (2022) AlphaFold Protein Structure Database: Massively expanding the structural
605 coverage of protein-sequence space with high-accuracy models. *Nucleic Acids Res* 50: D439–
606 D444
607 Wang C, Yang J, Song P, Zhang W, Lu Q, Yu Q & Jia G (2022) FIONA1 is an RNA N 6-
608 methyladenosine methyltransferase affecting Arabidopsis photomorphogenesis and flowering.
609 *Genome Biol* 23: 1–29
610 Wadsworth GM, Zahurancik WJ, Zeng X, Pullara P, Lai LB, Sidharthan V, Pappu R V., Gopalan V &
611 Banerjee PR (2023) RNAs undergo phase transitions with lower critical solution temperatures. *Nat*
612 *Chem* 15: 1693–1704
613 Wollman AJM & Leake MC (2015) Millisecond single-molecule localization microscopy combined
614 with convolution analysis and automated image segmentation to determine protein concentrations
615 in complexly structured , functional cells , one cell at a time. *Faraday Discuss* 00: 1–24
616 Wollman AJM, Shashkova S, Hedlund EG, Friemann R, Hohmann S & Leake MC (2017)
617 Transcription factor clusters regulate genes in eukaryotic cells. *Elife* 6: 1–36
618 Xu C, Wu Z, Duan HC, Fang X, Jia G & Dean C (2021) R-loop resolution promotes co-
619 transcriptional chromatin silencing. *Nat Commun* 12, 1790
620 Zhu P, Lister C & Dean C (2021) Cold-induced Arabidopsis FRIGIDA nuclear condensates for *FLC*
621 repression. *Nature* 599: 657–661
622

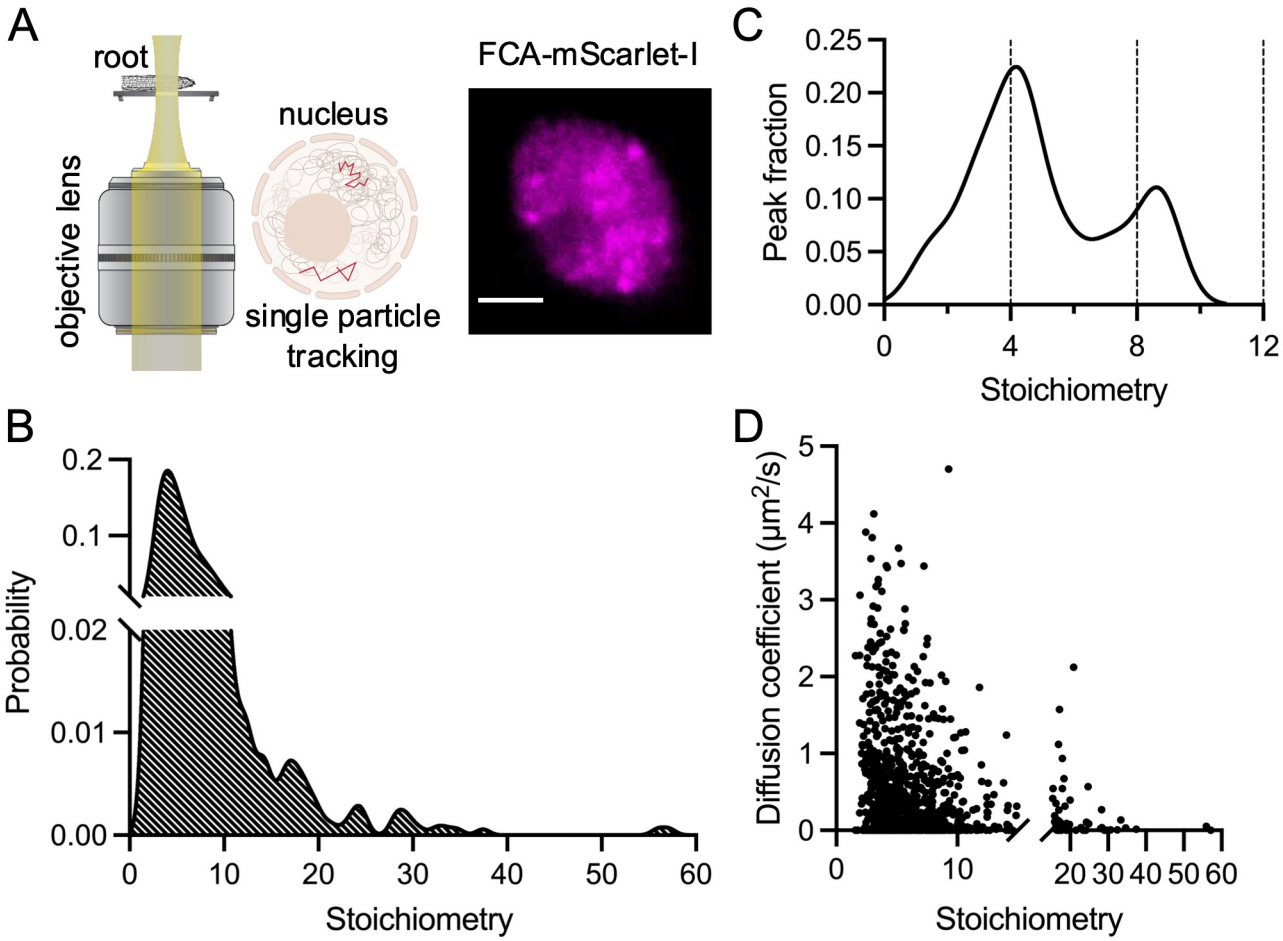

Figure 1. Super-resolution microscopy and single particle tracking to determine the physical properties of FCA condensates

A SlimVar microscopy of FCA-mScarlet-I (magenta) in Arabidopsis root cells. Scale bar, 2 μm.

B Distributions of stoichiometry (molecule number) of individual FCA particles.

C Periodicity of FCA particle stoichiometry estimated from the most common spacing between neighboring peaks in each stoichiometry distribution.

D The diffusion coefficient and stoichiometry of each FCA particle.

The single particle tracking analysis is from 3 biologically independent experiments. Results from individual replicate are provided in Appendix Figure S1.

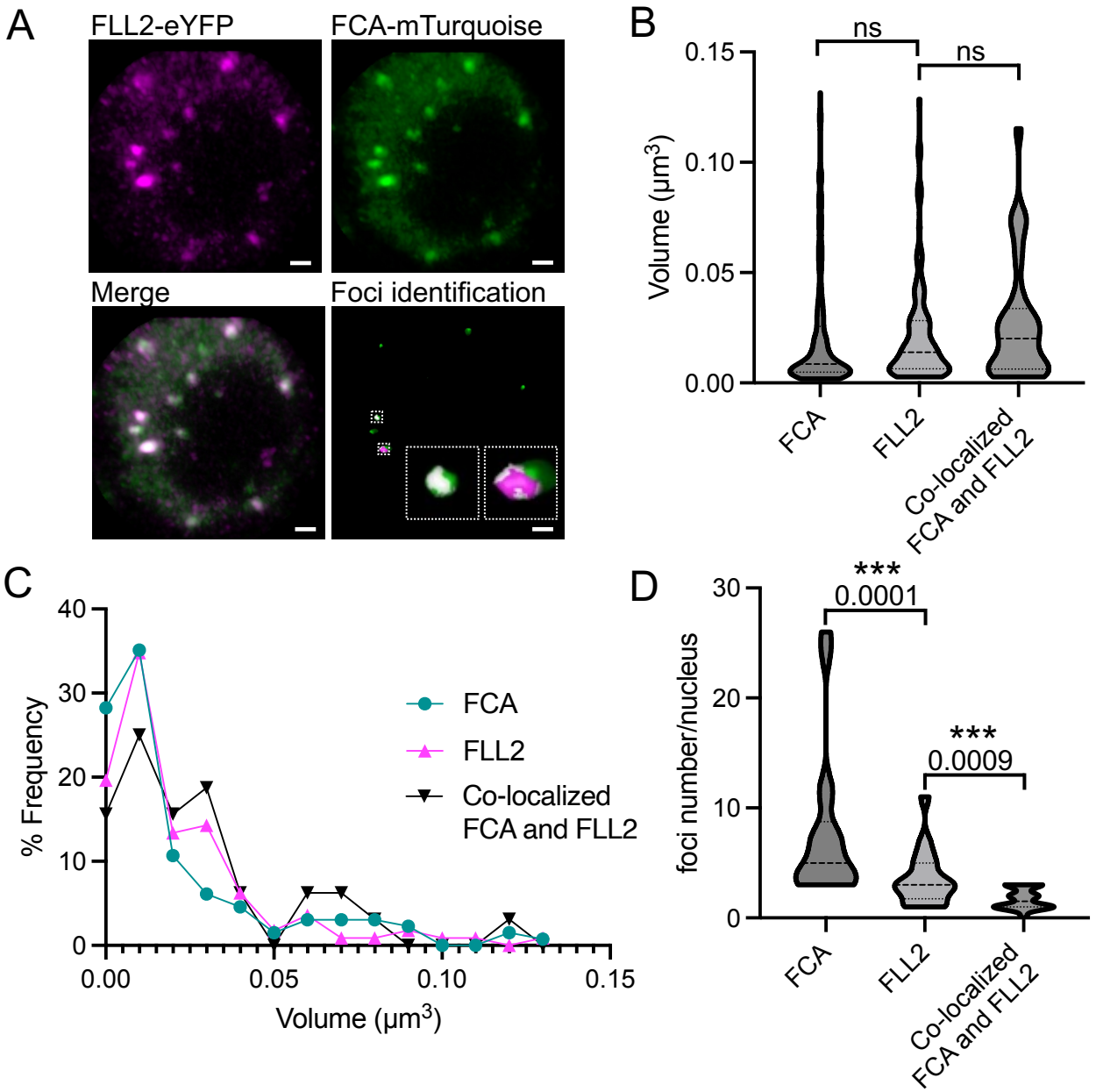

Figure 2. The co-localization of FCA and FLL2 is limited to larger sized condensates in Arabidopsis nuclei

A Representative 3D images of FCA and FLL2 colocalization. FCA-mTurquoise condensates (green) and FLL2 condensates (magenta) were imaged using Vision4D software. White areas indicate the co-localization of FCA with FLL2. The enlarged images of co-localized foci are shown in insets at the bottom right corner. Scale bars, 1 μm.

B Quantification of size of FCA, FLL2 and co-localized condensates. The lines in the violin plots indicate the median and quartiles. ns, no significance.

C Size and frequency distribution of FCA, FLL2 and co-localized condensates.

D Number of FCA, FLL2 or co-localized condensates in each nuclei. The lines in the violin plots indicate the median and quartiles. The quantitative analysis was based on 18 nuclei from 5 independent samples.

Statistical significance was determined using non-parametric Brunner-Munzel test. ***P-value < 0.001.

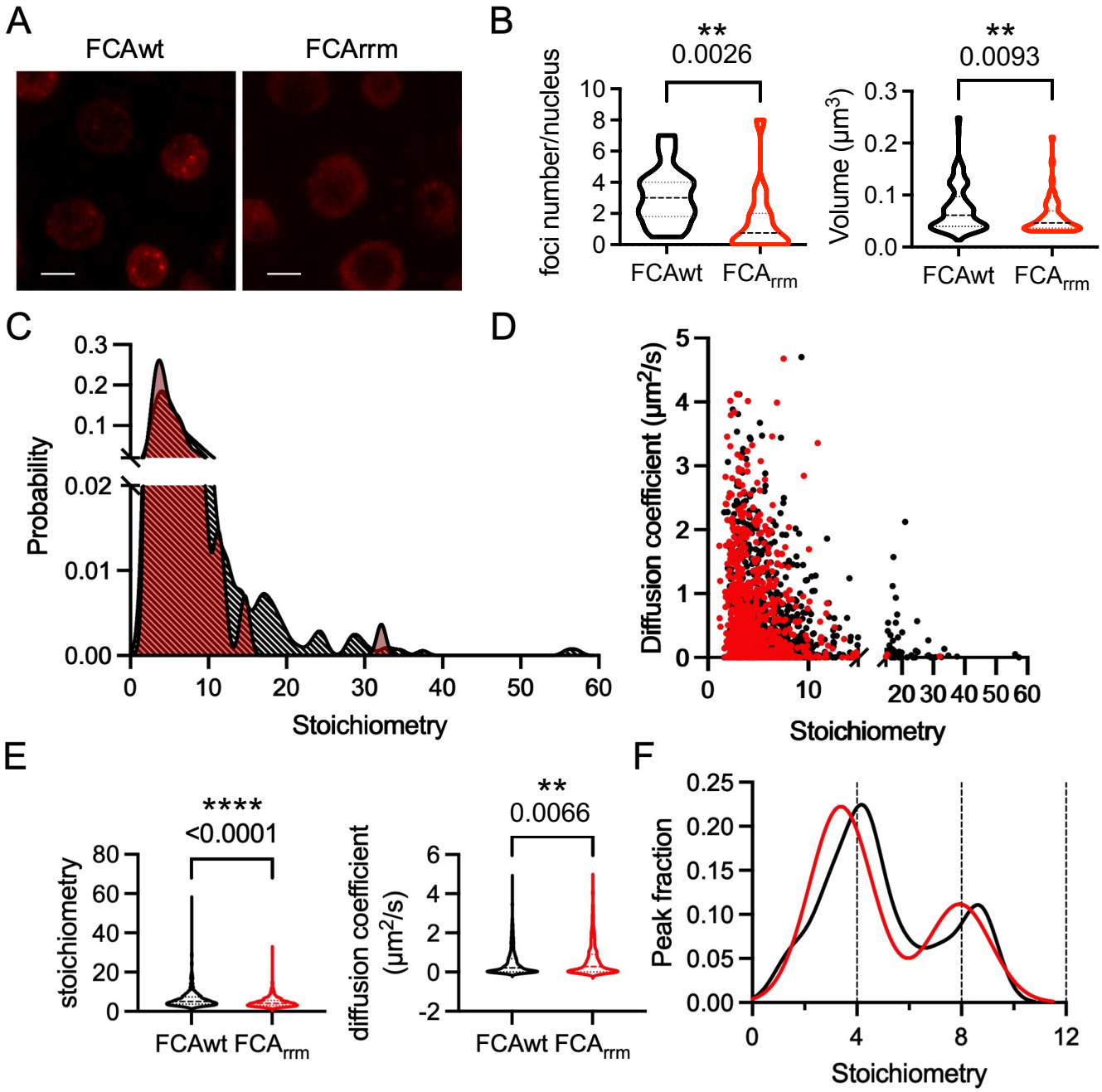

Figure 3. The RNA-binding activity of FCA influences FCA condensate size and number

A Representative Airyscan confocal images of wild type FCA fused to mScarlet-I (FCAwt) and FCA-mScarletI with the missense (L304F) mutation (FCArrm). Scale bars, 5 µm.

B Quantification of size and number of FCAwt and FCArrm condensates using Vision4D software. The lines in the violin plots indicate the median and quartiles. The quantitative analysis is based on 43 FCAwt nuclei and 65 FCArrm nuclei from 3 independent experiments.

C Distributions of stoichiometry of individual FCAwt (black) and FCArrm (red) particles.

D Diffusion coefficient and stoichiometry of each FCAwt (black) and FCArrm (red) particle.

E and F Statistic analysis of stoichiometry and diffusion coefficient of FCAwt and FCArrm particles. Periodicity of FCAwt (black) and FCArrm (red) particle stoichiometry. The single particle tracking analysis is from 3 biologically independent experiments. The FCAwt data corresponds to that shown in Figure 1.

Statistical significance was determined using non-parametric Brunner-Munzel test. ***P*-value < 0.01, *****P*-value < 0.0001. Results from individual replicates are provided in Appendix Figure S1 and S3.

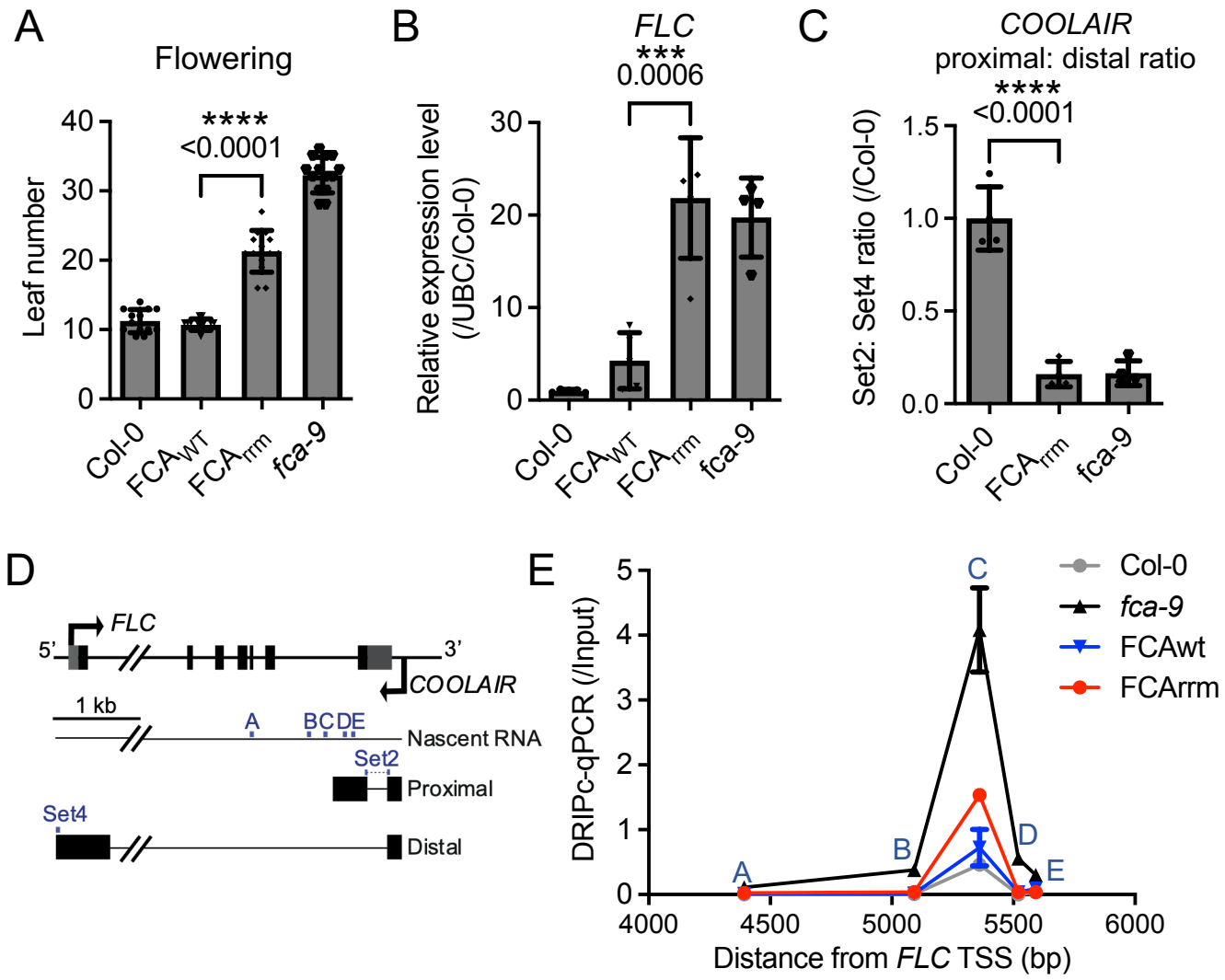

Figure 4. The missense mutation in the RRM of FCA only partially complements the *fca-9* mutant phenotype

A Flowering time of indicated plants grown in a long-day photoperiod. Data are presented as mean ± s.d. (n = 10).

B Expression of *FLC* relative to *UBC* in the indicated plants. Data are presented as mean ± s.d. (n = 5).

C The ratio of proximal: distal isoforms of *COOLAIR* transcripts relative to control (Col-0) in the indicated plants. Data are presented as mean ± s.d. (n = 4).

D Schematic of *FLC* and *COOLAIR* transcripts at the *FLC* locus. Blue dots indicate the locations of primer sets for qPCR. Untranslated regions are indicated by grey boxes, and exons by black boxes. kb, kilobase.

E DRIPc–qPCR analyzing *COOLAIR* R-loop in indicated genotypes. Data are mean ± s.d. from three biological replicates. TSS, transcription start site. The primer sets used for DRIPc-qPCR (A to E) corresponds to that shown in Figure 4D.

Statistical significance was calculated using the two-tailed t-test, with *P*-values indicated. ****P*-value < 0.001, *****P*-value < 0.0001.

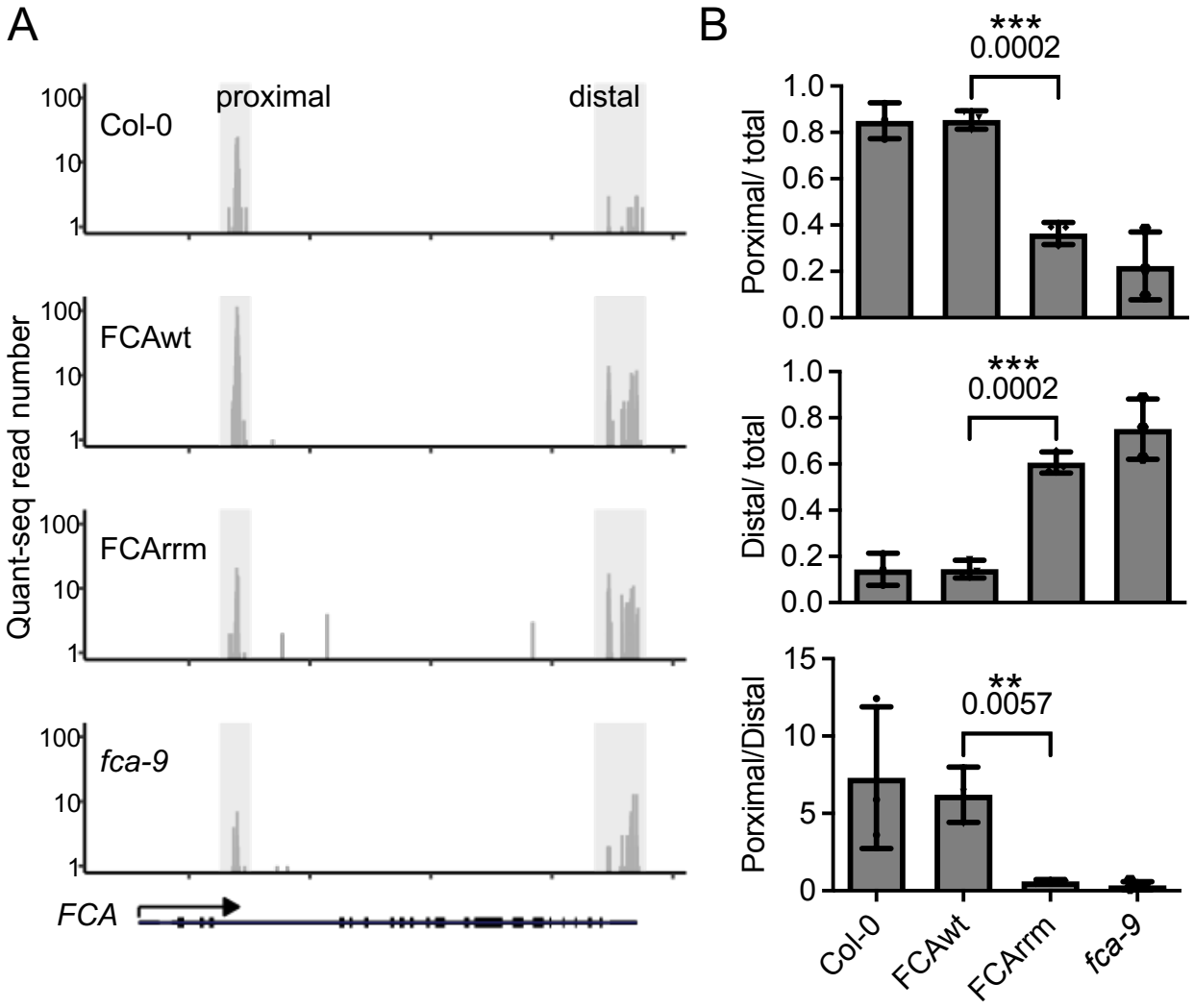

Figure 5. The functional FCA condensates are required for its autoregulation and RNA 3' processing

A Quant-seq experiments assaying polyA sites at the *FCA* locus in different genotypes. The vertical pale grey bars highlight previously described proximal and distal polyA sites.

B Quantification of reads corresponding to proximal and distal polyadenylated *FCA* transcripts. Data are presented as mean ± s.d. (n = 3).

Statistical significance was calculated using the two-tailed t-test, with *P*-values indicated. ***P*-value < 0.01, ****P*-value < 0.001.

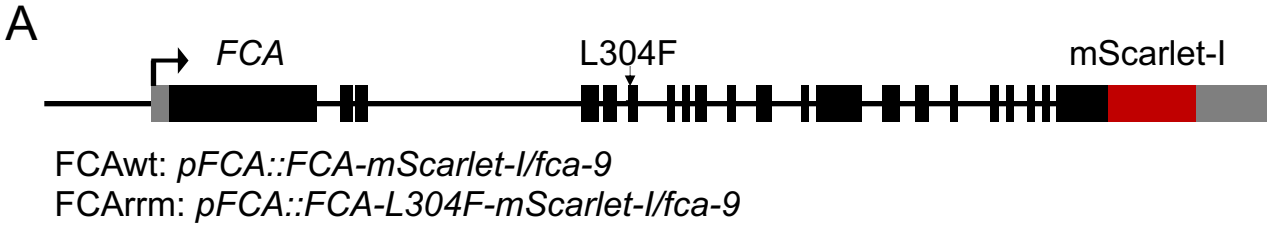
A
FCA
L304F
mScarlet-I
FCAwt: pFCA::FCA-mScarlet-I/fca-9
FCArrm: pFCA::FCA-L304F-mScarlet-I/fca-9

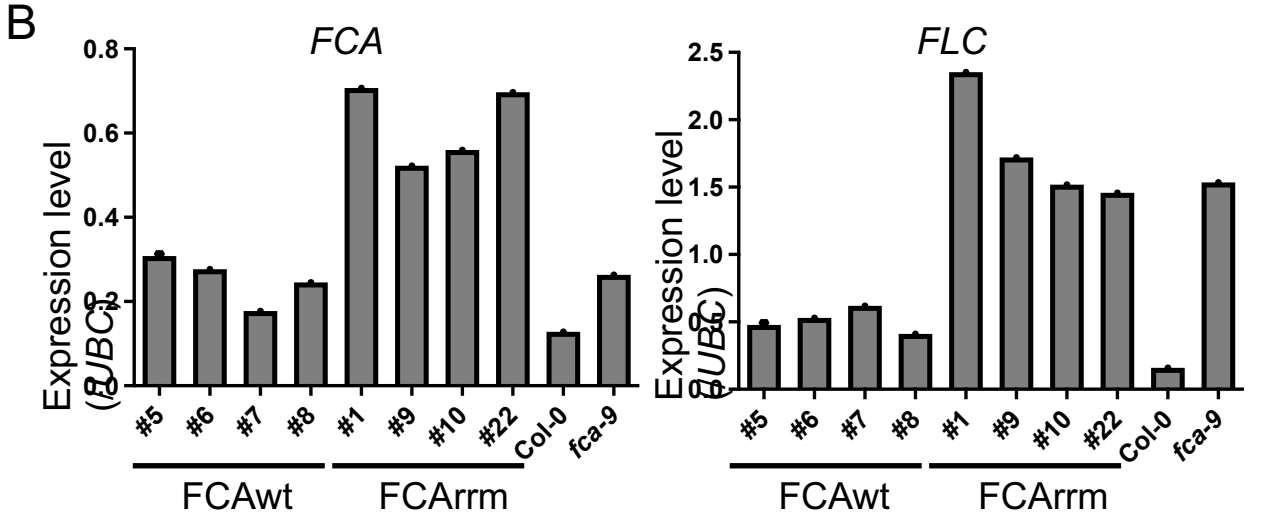
B
FCA
FLC
Expression level (AUBC)
0.8
0.6
0.4
0.2
0
2.5
2.0
1.5
1.0
#5
#6
#7
#8
#1
#9
#10
#22
Col-0
fca-9
FCAwt
FCArrm

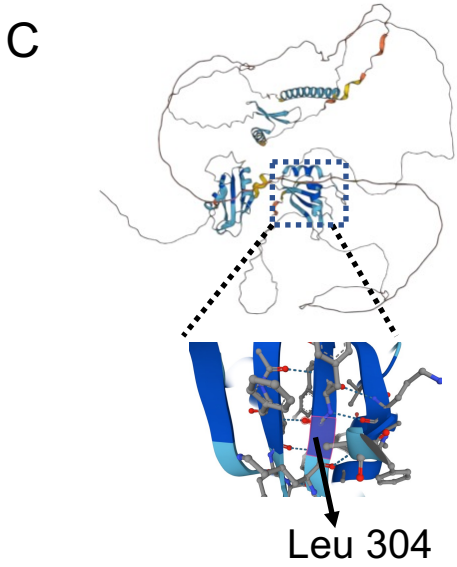
C
Leu 304

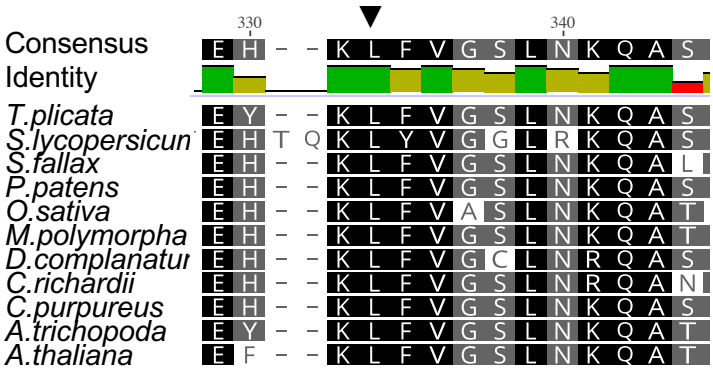
D
330
340
Consensus
Identity
T.plicata
S.lycopersicun
S.fallax
P.patens
O.sativa
M.polymorpha
D.complanatur
C.richardii
C.purpureus
A.trichopoda
A.thaliana

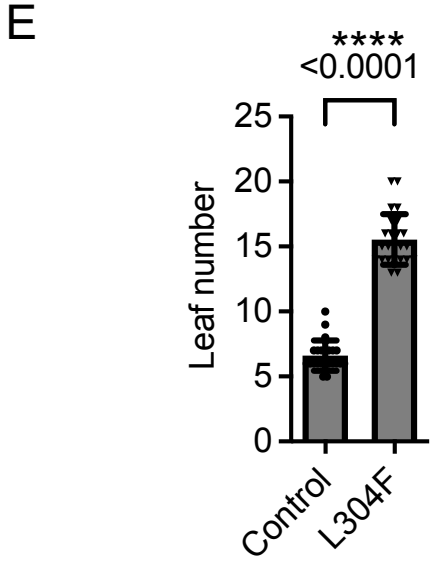
E
****
<0.0001
Leaf number
25
20
15
10
5
0
Control
L304F

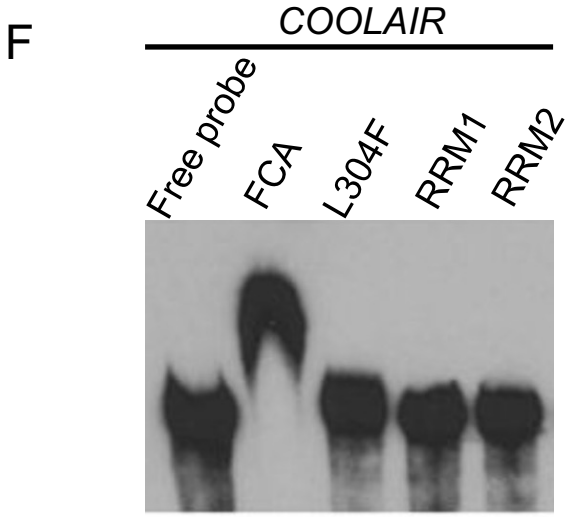
F
COOLAIR
Free probe
FCA
L304F
RRM1
RRM2

Figure EV1. A missense mutation (L304F) on the second RRM of FCA prevents RNA-binding

A Schematic representation of the transgenic FCA-mScarlet-I fusion within the FCA locus - the position of the missense L304F mutation is indicated. Untranslated regions are indicated by grey boxes, exon regions by black boxes, and mScarlet-I coding sequence by the red box.

B Expression of *FLC* and *FCA* relative to *UBC* in plants at the T3 generation following transformation. Data are mean values ± s.d. from pools of seedlings. The FCAwt #8 and FCArrm #1 lines are used for further analysis.

C FCA protein structure predicted by Alphafold Protein Structure Database (Q5I5A2). The arrow indicates the location of the amino acid change from the missense mutation.

D Peptide alignment of Arabidopsis FCA proteins from different plant species (https://phytozome-next.jgi.doe.gov). The arrow indicates the conserved Leucine 304.

E Plants carrying transgenes with the L304F mutation show delayed flowering compared to the control. Data are mean ± s.d. (n = 23 and 24 for the control and L304F, respectively). Statistical significance was calculated using the two-tailed t-test, with *P*-value indicated. ****P-value < 0.0001.

F *In vitro* RNA binding assay showing that the Leu 304 and each RRM domain are important.

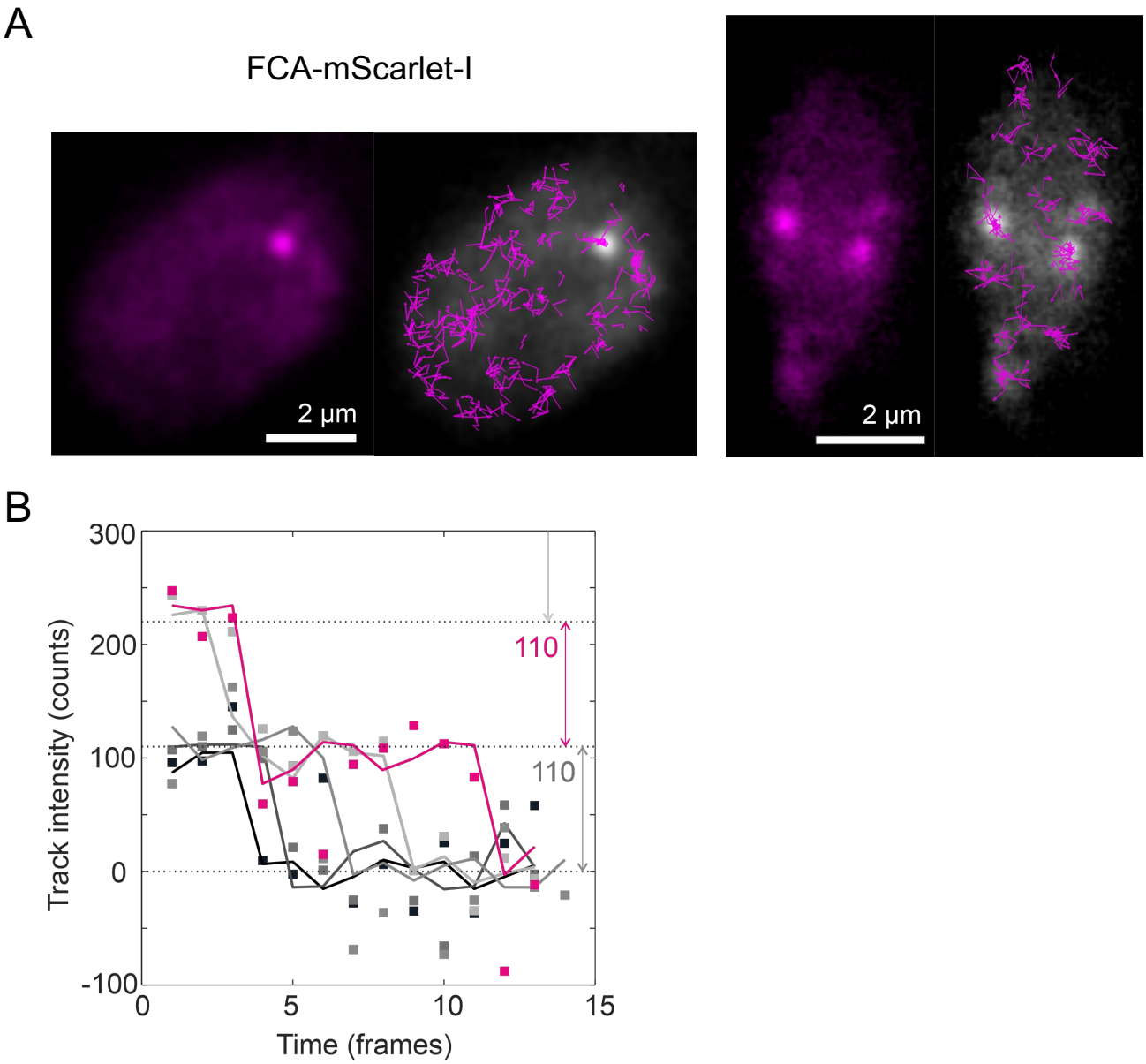

Figure EV2. Automated tracking analysis of FCA particles and determination of the characteristic single molecule brightness in living tissues.

A Two examples of FCA particle tracking achieve super-resolved localization precision and provide estimates of the corresponding stoichiometry and mobility.

B The consistent photobleaching steps yield an estimate of about 110 counts for the characteristic single-molecule brightness of the FCA-mScarlet-I *in planta*. The intensity of particles near the end of four particle tracks in the FCA-mScarlet-I image sequences is represented by square dots.

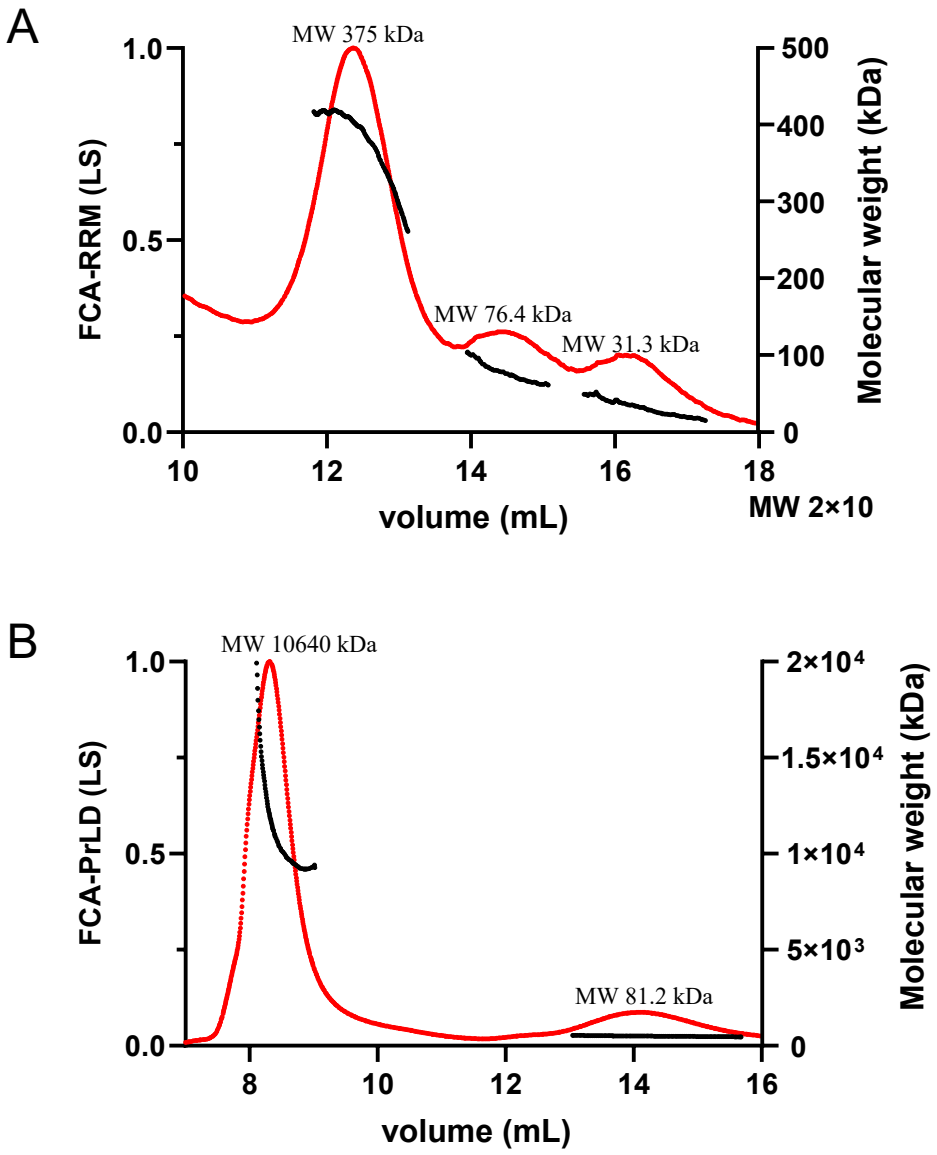

Figure EV3. SEC-MALS of purified FCA truncated proteins
SEC-MALS of purified FCA-RRM (A) or FCA-PrLD (B). Line traces indicate molar masses as derived from MALS. The predicted molecular masses of FCA-RRM and FCA-PrLD are approximately 110 kDa and 100 kDa, respectively.

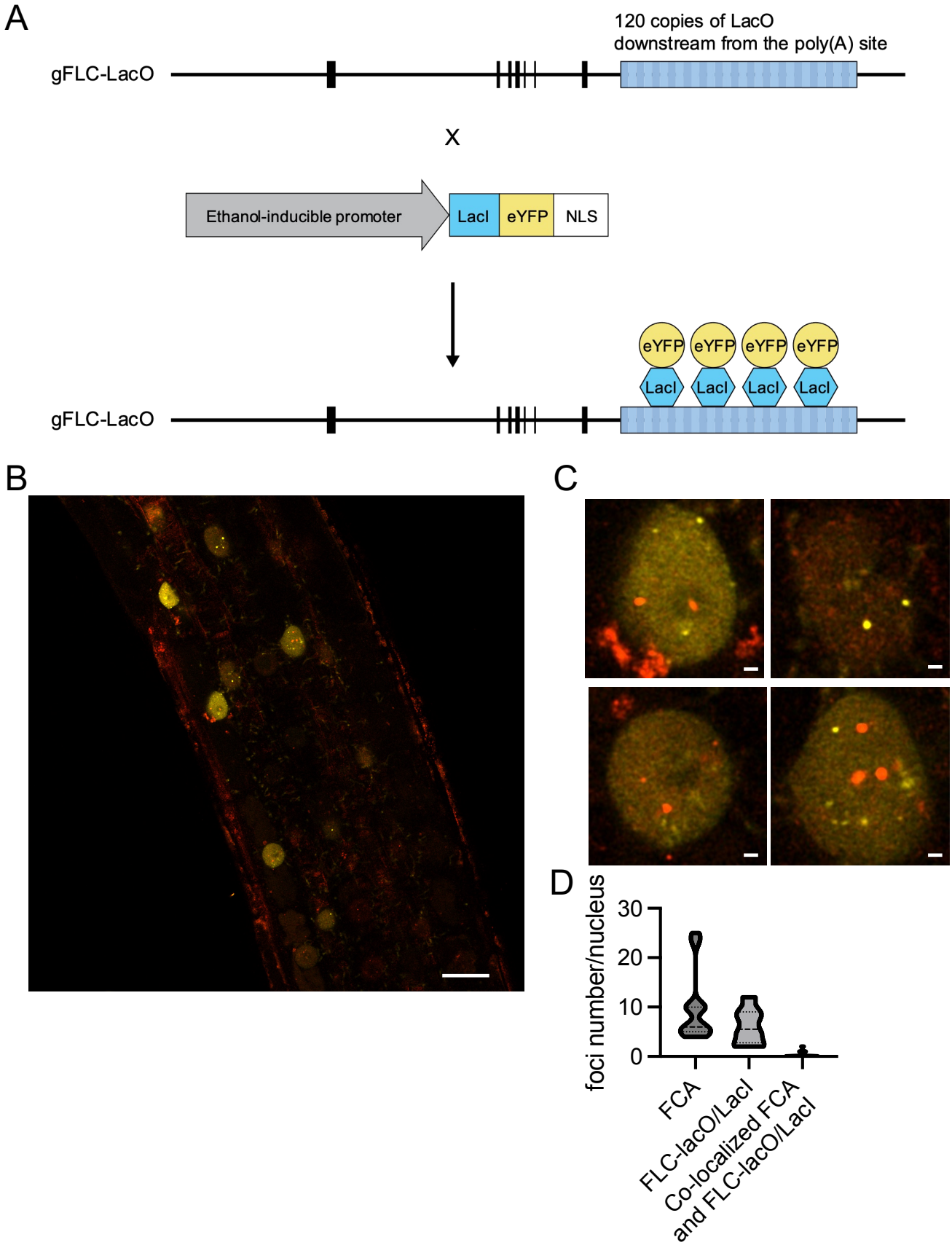

Figure EV4. Co-localization of FCA condensates and *FLC-lacO*/LacI-eYFP

A An illustration of the *FLC-lacO*/LacI-eYFP transgenic plants.

B Single slice of Arabidopsis root Airyscan image showing expression of FCA-mScarlet-I (red) and *FLC-lacO*/LacI-eYFP (yellow) in nuclei. Scale bars, 20 µm.

C Subsets of Airyscan images from B showing nuclei co-expressing FCA condensates (red) and *FLC-lacO*/LacI-eYFP (yellow). Scale bars, 1 µm.

D Quantification of condensate number of FCA, *FLC-lacO*/LacI-eYFP or co-localized foci in nuclei from 3D Airyscan images. The quantitative analysis is based on 18 nuclei.

The images were acquired on a Zeiss LSM980 using LD C-Apochromat 40x/NA 1.1 water-immersion objective or C-Apochromat 63x/NA 1.2 water-immersion objective. The fluorescent probes, eYFP and mScarlet-I, were excited at 488 and 561 nm, respectively. The voxel size of images for quantification analysis was 0.05 µmx 0.05 µmx 0.21 µm (xyz).